



OPEN

# Synchrotron nano-FTIR spectroscopy for probing anticancer drugs at subcellular scale

Luis A. E. Batista de Carvalho<sup>1</sup>, Gianfelice Cinque<sup>2,4</sup>, Ana L. M. Batista de Carvalho<sup>1</sup>, Joana Marques<sup>1</sup>, Mark D. Frogley<sup>2</sup>, Hendrik Vondracek<sup>2</sup> & Maria Paula M. Marques<sup>1,3</sup>

The cellular response to cisplatin was assessed in human osteosarcoma cells, using synchrotron-based (SR) Fourier Transform InfraRed nanospectroscopy (nano-FTIR) at the MIRIAM beamline B22 of Diamond Light Source (UK). This label-free mapping method delivered simultaneous morphological and biochemical information on a subcellular level (i.e. 100 s nanometer or better). Based on specific spectral biomarkers, the main biochemical constituents affected by the drug were identified at distinct locations within the cell's inner body. Cisplatin was shown to have a noteworthy effect on proteins, mostly within the cytoplasm. A clear drug impact on cellular lipids was also observed. Within current literature on s-SNOM, this nanospectroscopy work represents a first successful application in life sciences providing full fingerprint nano-FTIR spectra across intact human cancer cells.

**Keywords** Nanospectroscopy, Nano-Fourier Transform Infrared (nano-FTIR), Synchrotron Radiation (SR), Osteosarcoma, Cisplatin, Scattering-Scanning Near field Optical Microscopy (s-SNOM)

Osteosarcoma is a cancer with a poor prognosis, incident mainly among children and adolescents, for which new and more effective chemotherapy strategies are urgently needed<sup>1</sup>. At present, high-grade osteosarcoma is mainly treated with DNA-damaging agents such as cisplatin (*cis*-(NH<sub>3</sub>)<sub>2</sub>PtCl<sub>2</sub>), which was introduced to the clinics in the late 1960's as the first anticancer metallodrug<sup>2-4</sup>. Its antineoplastic activity is hindered by low bioavailability, toxicity and acquired resistance which greatly undermine chemotherapy success<sup>5</sup>. A better understanding of the drug's *ex vivo*/*in vitro* mode of action, particularly regarding its biological impact at the cellular and subcellular levels, is therefore crucial for increasing its effectiveness and improving patient outcome.

Previous studies by synchrotron-based Fourier Transform IR microspectroscopy (SR micro-FTIR), micro-Raman and inelastic neutron scattering (INS), yielded relevant results on the drugs' metabolic effect and cellular response to chemotherapy, but they did not allow access to the effect on specific sub-cellular regions<sup>6-11</sup>. The present work applies SR nano-FTIR as an innovative way of probing the effect of cisplatin within human osteosarcoma cells, targeting the organelle scale at a resolution better than 100 nm, and spatial sampling (step size) between 200 and 500 nm to cover an entire cell. This type of information is paramount for understanding the cytotoxicity pathways of anticancer agents and therefore to achieve an improved efficacy, sensitivity, and specificity. The current experiment constitutes the first life sciences application of scattering- Scanning Near-field Optical Microscopy (s-SNOM) at Diamond Light Source (UK). By revealing the action of a consolidated metallodrug at the subcellular scale, the results of this study are expected to foster the development of novel metal-based chemotherapeutic agents against osteosarcoma, which is a pressing clinical need.

IR Nanospectroscopy (nano-FTIR) combines s-SNOM with infrared illumination and FTIR-based spectral detection<sup>12-14</sup>. When the infrared beam is focussed at the interface of the sample surface and the atomic force microscope (AFM) tip, the local IR electric field is enhanced non-linearly between the tip and reflective sample substrate. By modulating the tip-sample distance using the intermittent contact, or *tapping* mode of the AFM, lock-in amplification can then be used to detect the near-field components of the scattered light from the region

<sup>1</sup>Department of Chemistry, Química-Física Molecular, University of Coimbra, 3004-535 Coimbra, Portugal. <sup>2</sup>Diamond Light Source, Harwell Science and Innovation Campus, Chilton - Didcot OX11 0DE, Oxfordshire, UK. <sup>3</sup>Department of Life Sciences, University of Coimbra, 3000-456 Coimbra, Portugal. <sup>4</sup>Department of Engineering Science, University of Oxford, Oxford OX1 3PJ, UK. ✉email: gianfelice.cinque@diamond.ac.uk; gianfelice.cinque@engs.ox.ac.uk; almbc@uc.pt

within tens to a few hundred of nanometres around the tip, overcoming the resolution limits of micro-FTIR spectroscopy due to the optical diffraction limit. Hence, nano-FTIR provides the label-free chemical analysis capability of FTIR coupled to the extremely high spatial resolution given by s-SNOM, as already applied in life science studies<sup>15–18</sup>. When coupled to the broad bandwidth and brightness of synchrotron IR radiation, it becomes a tool of choice for in situ spectroscopy and mapping of tissue and cellular constituents, as well as for monitoring drug distribution and drug-biomolecule interactions, providing both morphological and biochemical information in the same experiment<sup>19–22</sup>. Among the strong points of Synchrotron Radiation (SR) in nano-FTIR we count the unique spectral broadness, seamless IR coverage, high stability and a diffraction limited spot size at the sample, ideal for non-destructive nanospectroscopy of *e.g.* biosamples.

## Materials and methods

### Cell culture and sample preparation

Human osteosarcoma MG-63 cells were grown as monolayers at 37 °C, in a humidified atmosphere of 5% CO<sub>2</sub>, in a DMEM-HG medium supplemented with 10% (*v/v*) heat-inactivated FBS, 1% (*v/v*) penicillin (100 U mL<sup>-1</sup>)/streptomycin (100 mg mL<sup>-1</sup>) and sodium bicarbonate-20 mM (pH 7.4). Upon harvesting by trypsinization (at 80% confluence), the cells were centrifuged, and the pellet was resuspended in culture medium, then seeded onto Au-coated silicon substrates (10 × 10 mm<sup>2</sup>), at a concentration of 5 × 10<sup>4</sup> cells/cm<sup>2</sup> (prepared at University of Coimbra). After incubation for 48 h (allowing the cells to attach), the tested drug (cisplatin) was added at a 12 μM concentration, and the cells were allowed to grow for a further 48 h. This drug dosage and incubation period (IC<sub>50</sub> at 48 h) were previously optimised for this type of cells<sup>23,24</sup>. The growth medium was removed, the cells were washed twice with 0.9% NaCl (*w/v*), formalin-fixed according to published procedures<sup>8</sup>, and washed several times with de-ionized water (to remove any residual salt). Prior to spectroscopic analysis, the substrates were allowed to air-dry. All samples were prepared in duplicate, in a single experiment.

### Synchrotron-based nano-FTIR spectroscopy

SR nano-FTIR data were obtained on formalin-fixed human osteosarcoma MG-63 cells, with and without cisplatin added in the culturing phase. Topography, *whitelight* (i.e. total intensity) infrared maps and mechanical response (tapping amplitude and phase) images were acquired by AFM tapping in s-SNOM mode, at the new nanoIR endstation of the MIRIAM beamline (B22) of the Diamond Light Source, UK<sup>25,26</sup> using a s-SNOM setup (Neaspec/Attocube GmbH, Munich, Germany). This instrument comprises an AFM tip as a near-field probe, illuminated by the broadband synchrotron radiation of the beamline. The scattered IR signal from the tip-sample interface is detected by a liquid nitrogen-cooled, high sensitivity, mercury cadmium telluride (MCT) detector, to yield IR amplitude and phase information (related to local reflectivity and absorption spectra, respectively), with a spatial resolution in the range 10 to 100 nm<sup>27,28</sup>. The cells were seeded on Au-coated substrates which, due to the strongly reflecting properties and biochemical compatibility, allow an enhanced near-field infrared signal along with good cell adherence.

FTIR acquisition was performed within the 650–4000 cm<sup>-1</sup> region, via the nanoIR endstation equipped with a ZnSe beamsplitter in an asymmetric Michelson interferometer. Experimentally, nano-FTIR spectra of cells were measurable with sufficient signal quality in the fingerprint region, thus the focus of this study is in the 600 cm<sup>-1</sup> to 1800 cm<sup>-1</sup> IR range. Topography, IR scattering amplitude and phase up to the 4th harmonic were detected simultaneously, at selected locations within each cell, using the s-SNOM tapping mode at a tapping amplitude of *ca.* 100 nm, by a PtIr-coated AFM tip oscillating vertically (setpoint circa 80%) at the lowest mechanical resonance frequency of the cantilever (*ca.* 70 kHz). The synchrotron IR beam was incident at a shallow angle onto the sample plane. Images and spectra at the first and higher harmonics of the cantilever mode were acquired. In this work we present the second harmonic maps and spectra only, as they represent an effective compromise between near-field signal intensity and spatial resolution. Spectra were obtained by averaging 100 interferograms, for an integration time of 10 ms *per* point of each interferogram which contains 500 points, at a spectral resolution of 10 cm<sup>-1</sup>, and were normalised to a background scan acquired on a Si substrate (collected before each new sample measurement). Line scans across the cells were also obtained, at step sizes up to 500 nm (from 30 to 90 points per line) in order to cover the whole cell dimension. Each spectrum (at each cellular location) took *ca.* 10 min of acquisition time for an acceptable signal-to-noise ratio (S/N), and line scans took between 5 to 15 h. During the experiments, cells were studied after treatment with different reagents and at different concentrations. For the system considered here, point spectra and a linescan were performed for a concentration of 12 μM of cisplatin on a single cell. For the controls, four cells were probed, measuring point spectra and linescans and only datasets with sufficient spectral quality were considered for further analysis.

To avoid artefacts, the AFM tips were regularly changed (as soon as any degradation in the topography map was visible). At the MIRIAM beamline B22 of Diamond the beam intensity reaching the sample is about 1 mW (integrated over the whole mid-IR range), which ensures there is no significant sample heating or radiation damage to the mammalian cells.

Recorded spectra were analysed using Quasar 1.9.0<sup>29</sup>. A rubber-band baseline correction of the phase signal was performed, followed by a Savitzky-Golay smoothing of the data, based on a 2nd order polynomial (window size 15 points) on data after post zero filling (equivalent to a spectral step of 2.5 cm<sup>-1</sup>). In order to better assess spectroscopic differences in different parts of the cell, k-means clustering analysis was performed on the nanoIR spectra of each of the samples (control and drug-treated) separately. Three (drug-treated) and two (control) clusters were clearly identified with the highest silhouette score after removing, in total, three spectra that were spectral outliers.

## Results and discussion

Synchrotron-based nano-FTIR measurements were carried out for both drug-free (control) and cisplatin-exposed human osteosarcoma cells (MG-63 cell line). For the latter, a drug concentration of 12  $\mu\text{M}$  was used, for an incubation time of 48 h, in agreement with the corresponding 50% cell growth inhibition (IC50) values formerly determined by the authors for cisplatin-like Pd-compounds<sup>23</sup>, and to allow for a better comparison of various drugs. Topography, mechanical response and optical images were obtained simultaneously (the optical amplitude and phase being directly correlated to the sample's IR reflection and absorption, respectively), revealing a high sub-cellular heterogeneity at the nanometre scale (Fig. 1A–C). Although the features detected by nano-FTIR arise mainly from chemical differences (IR absorption), it is worth noting that in s-SNOM the phase signal is interpreted as an absorption in a linearized approximation valid for thin and low absorbing samples. The cellular images show well resolved cell and organelle contours, demonstrating the very good adherence of the MG-63 cells to the Au-coated substrate, as well as the effectiveness of the fixation procedure. An additional example of a control cell measured by nano-FTIR/s-SNOM can be found in the Supplementary information Fig. 3.

Cell thicknesses up to 0.8  $\mu\text{m}$  were measured for the formalin-fixed cells under study (typical for this class of samples<sup>30,31</sup>), with differences observed across the cell. A maximum thickness was recorded near the nucleus, a particularly dense organelle surrounded by the less dense cytosol (Fig. 1D). As expected, the signal-to-noise ratio obtained by nano-FTIR is intrinsically lower than the one corresponding to a micro-FTIR experiment, since the probed area is much smaller for the former (*ca.* 4 orders of magnitude). The nano-FTIR signal is only detectable thanks to the enhancement due to the antenna effect of the AFM tip. As shown in Fig. 2, key spectral information is gained by nano-FTIR in the important spectral region below 1000  $\text{cm}^{-1}$  (*e.g.* bands ascribed to phosphate groups or backbone modes of DNA), as the near-field signal is further enhanced at longer wavelengths with respect to the typical diffraction limit constraints given by micro-FTIR in transmission when using optical microscopy and optical slits below 10  $\mu\text{m}$ .

s-SNOM is mostly a surface-sensitive technique, and nano-FTIR is ideal for thin sample thicknesses on a 100 nm scale<sup>32</sup>. The nano-FTIR experiments currently carried out in the mid-IR region were performed using a highly reflective substrate, in order to enhance the s-SNOM signal from the cell. In general, the penetration depth is sufficient to probe cell constituents beyond the cell membrane, such as the nucleus (plus nucleoli) and lipid droplets. The nano-FTIR spectral profiles comprised bands from the main cellular components (Fig. 2A, Table 1): proteins (Amide I and II bands at 1650 and 1540  $\text{cm}^{-1}$  respectively), lipids (*e.g.*  $\delta(\text{CH}_2)$  at 1440–1460  $\text{cm}^{-1}$ ) and DNA/RNA (*e.g.*  $\nu(\text{CC})$ ,  $\nu(\text{CO})$ ,  $\nu(\text{OPO})_{\text{backbone}}$  and  $\nu(\text{PO}_2)$ , at 780, 960, 1046 and 1245  $\text{cm}^{-1}$ )<sup>6</sup>. The detection of characteristic IR signals from DNA gives clear evidence that the nano-FTIR is probing below the cellular

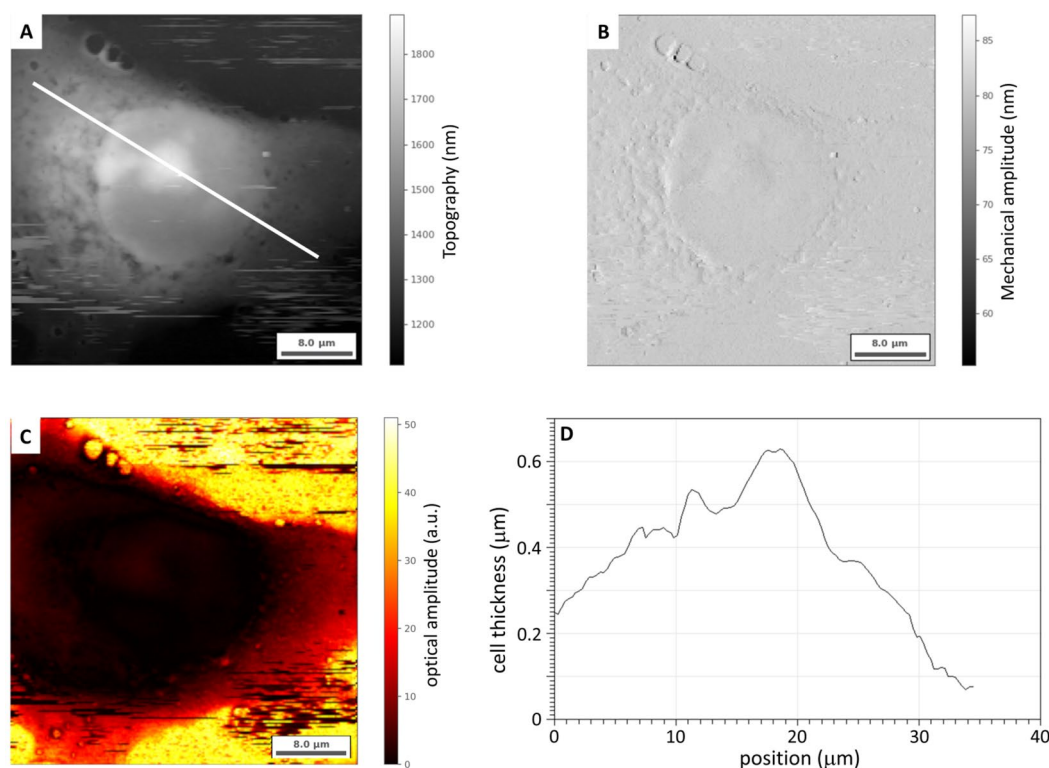


**Figure 1.** Images of a human osteosarcoma cell (MG-63, formalin-fixed), obtained by synchrotron-radiation nano-FTIR spectroscopy: (A)—AFM topography; (B)—mechanical tapping amplitude; (C)—IR scattering image (optical amplitude, second harmonic). (D)—AFM-derived cell thickness along the line depicted in (A).

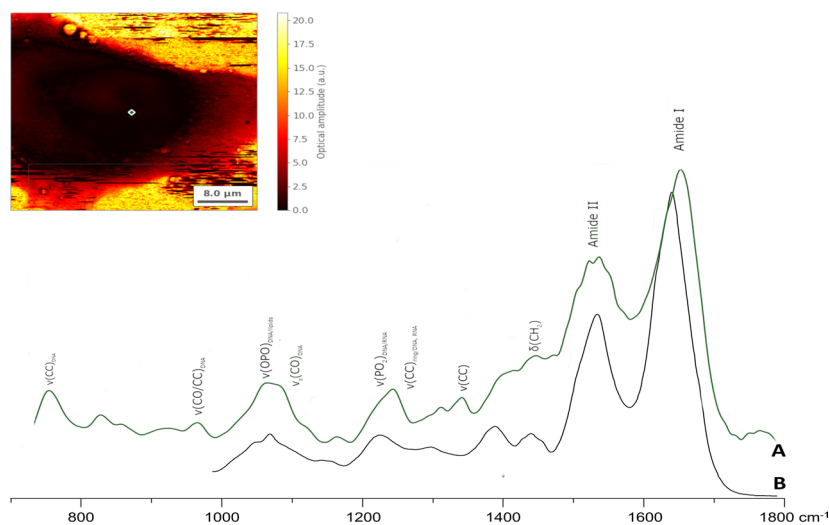


**Figure 2.** FTIR spectra of human osteosarcoma cells (MG-63, formalin-fixed): (curve A) synchrotron-radiation nano-FTIR spectrum, cells grown onto Au-coated substrates, collected at the spot shown in the infrared image of the cell (spectral data averaged over 21 spectra recorded at the same point); (curve B) synchrotron-radiation micro-FTIR average spectrum, cells grown on CaF<sub>2</sub> disks<sup>8</sup>. Inset: nano-IR *whitelight* image of the cell, showing the point where spectrum (A) was acquired.

Drug-free	Drug-exposed	<sup>a</sup> Assignment
Wavenumber (cm <sup>-1</sup> )	Wavenumber (cm <sup>-1</sup> )	
781	778	v(CC) <sub>DNA</sub>
967	977	v(CC)/v(CO) <sub>DNA</sub>
1052, 1086	1066	v(OPO) <sub>DNA,lipids</sub> , v(C-OH) <sub>carbohyd</sub>
1129	1136	v(CO) <sub>DNA-deoxyrib</sub> , v(CN)/v(CO)
1171	1166	v(CO) <sub>DNA</sub>
1246	1242	v <sub>as</sub> (PO <sub>2</sub> ) <sub>DNA</sub> , v(CN)/v(CO)/v(CC) <sub>DNA</sub> , Amide III
1280	1284	v(CC) <sub>DNA</sub> , δ(C=C) <sub>lipids</sub>
	1337	v(CC) <sub>DNA</sub> , δ(CH <sub>2</sub> )
<b>1465</b>	<b>1446</b>	<b>δ(CH<sub>2</sub>)</b>
	1503	δ(CH <sub>2</sub> ), v(CC)
	1521	v(CC)
1546	1539	Amide II, v(C=C)
<b>1657</b>	<b>1633</b>	<b>δ(C=CH), v(C=C) Amide I</b>
1668	1656	δ(NH <sub>2</sub> ), v(C=O) <sub>proteins</sub> , δ(C=C) <sub>lipids</sub> , Amide I
1733	1748	v(C=O) <sub>ester</sub>

**Table 1.** Experimental nanoIR vibrational wavenumbers (cm<sup>-1</sup>) and band assignments<sup>6</sup>, for human osteosarcoma MG-63 cells, before and after drug exposure (cisplatin-12 μM, for 48 h). In bold the bands with a significant shift i.e. greater than the spectral resolution used. <sup>a</sup>v—stretching; δ—deformation; s—symmetric; as—anti-symmetric; carbohyd—carbohydrates; deoxyrib—deoxyribose; Amide III, Amide II—(δ(CN-H) + v(CN))<sub>proteins</sub>; Amide I—v(C=O)<sub>proteins</sub>.

membrane. Several significant spectral bands can be identified in comparison to the micro-FTIR data previously reported for the same MG-63 cells, measured by transmission far-field SR micro-FTIR<sup>8</sup> (Fig. 2 (curve B)).

Subcellular IR mapping was attained, unveiling the impact of cisplatin on cellular proteins and lipids, as well as on DNA, which was evidenced, respectively, by significant changes in: Amide I/Amide II protein bands; CH<sub>2</sub> deformations (mainly from lipids); and v(CO) (from DNA) (Fig. 3). Negative bands at about 806, 1000–1100 and 1265 cm<sup>-1</sup> in these spectra are attributed to a contamination of the AFM tips with PDMS affecting the background, as previously observed by Bechtel et al.<sup>33</sup> (polymer present in tips packaging). Independently of these artefacts, the spectra are otherwise consistent with former micro-FTIR and micro-Raman data obtained by the authors for cisplatin-treated breast cancer cells<sup>6,9,10</sup>.

SR nano-FTIR data was collected sequentially along a line across both control (drug-free) and Cisplatin-exposed cells, revealing variations in chemical composition within the cellular milieu, at distinct cellular regions—membrane, cytoplasm or nucleus (Fig. 4).

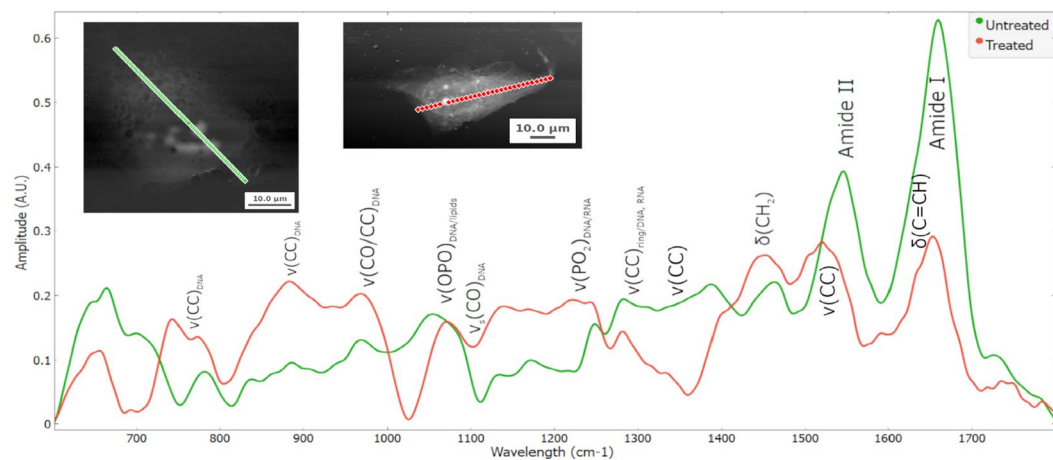


**Figure 3.** Synchrotron-radiation nano-FTIR spectra, for human osteosarcoma cells (MG-63, formalin-fixed) both untreated and treated with cisplatin, averaged over all the points of the linescans shown in corresponding topographic images (inset).

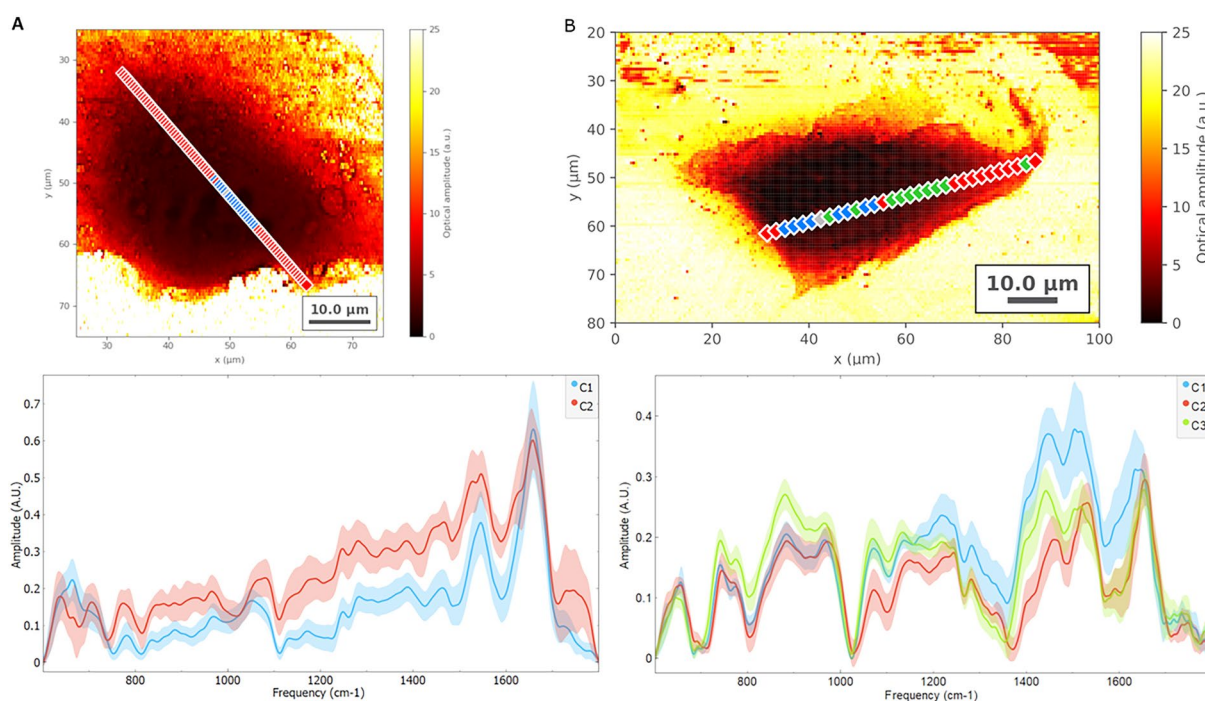


**Figure 4.** Synchrotron-radiation nano-FTIR spectroscopic linescans across human osteosarcoma cells (MG-63, formalin-fixed): (A) control (drug-free) with 90 points; (B) cisplatin-exposed (12  $\mu\text{M}$ , 48 h) with 31 points. The colour coded image shows the overall O2A signal of the cell. k-means clustering analyses were performed on the respective series of spectra, and 2 (on control) or 3 (on drug-treated sample) clusters were identified. The points of the linescans are colour coded according to the assigned clusters. The corresponding average spectra (bold line), including variance, are shown below.

Separate k-means cluster analyses were performed for the control and drug exposed cells and two (control) or three (drug-exposed) distinct clusters were identified (Fig. 4), corresponding to different numbers of spectra: for the control 79 spectra are within C1 and 10 within C2, and one spectrum was discarded due to a high level of noise; for the treated cells, 15 spectra are within C1, 11 within C2 and 4 within C3. Regarding the cisplatin-treated samples, the initial k-means analysis gave 4 clusters. However, since C4 was found to have only one spectrum (displaying a strong feature centred at *ca.* 1340  $\text{cm}^{-1}$ ) it was considered an outlier and removed from the overall representation. More details are provided in the SI document.

Signals from DNA and lipids were clearly detected in both the drug-exposed and the drug-free cells. The characteristic features from proteins (Amide I and Amide II) were distinctly observed for the control sample (across the whole cell) (Fig. 4A), while they could only be detected at specific cellular locations in the drug-treated

cell (Fig. 4B). In the drug-exposed cell, cluster C2 (mostly from the cellular border) displayed the Amide I and Amide II signals (at 1650 and 1550  $\text{cm}^{-1}$ , respectively), while spectra from the cytoplasm (cluster C3) exhibited a significant variation of the  $\text{CH}_2$  deformation modes (at *ca.* 1450  $\text{cm}^{-1}$ , mainly from lipids and proteins). Cluster C1, corresponding to the perinuclear region, showed the most distinctive changes in the protein bands, as well as the presence of DNA (phosphate and ring modes) and lipids (both saturated and unsaturated—bands at 800–1320  $\text{cm}^{-1}$ , and 1420–1500  $\text{cm}^{-129}$ , respectively). This chemical heterogeneity, namely the inhomogeneous protein distribution within drug-incubated cells, has been previously observed by photothermal nanospectroscopy in human cervix adenocarcinoma (HeLa) cells<sup>30</sup>. Overall, the spectral profiles currently obtained for drug-free and cisplatin-exposed cells revealed a clear drug impact on the cellular proteins, as well as on the lipids and DNA.

Furthermore, features at *ca.* 1756 and 1742  $\text{cm}^{-1}$  (for control and cisplatin-containing cells, respectively) were assigned to fatty acid esters (Table 1), and detected both for the drug-free and drug-treated cells, mainly in thinner regions of the cells (Fig. 4A,B). These are therefore suggested to be due to the lipidic components of the cellular membrane or to lipid droplets within the cytoplasm. Additionally, the bands between 1424 and 1503  $\text{cm}^{-1}$  show high intensity in all clusters from the cisplatin-treated cells (Fig. 4B), and are significantly less intense in the control samples (Fig. 4A): they are assigned to the  $\delta(\text{CH}_2)$  modes of aliphatic chains mainly from fatty acids, but also have contributions from proteins and carbohydrates<sup>34–36</sup>.

The cell's morphology can also be inferred from their AFM-derived images (Fig. 5A), from which it is possible to retrieve the cell thickness along the scanned area (Fig. 5B). Morphology may be directly correlated with the cellular chemical composition, which is an added value of these type of AFM-nano-FTIR experiments. There was an evident increase in cell thickness in the nuclear region of the cell, either in the presence or absence of cisplatin, but this cell thickness variation along the cell width yielded quite distinct profiles for drug-free and drug-treated samples (Fig. 1D vs Fig. 5B), revealing a noticeable drug effect on cell's morphology (apart from cell's biochemical composition): there is a much more gradual thickness change along the cell for the non-treated as compared to the treated cells—*ca.* 130 nm increase at the nucleus, with an overall maximum height of 550 nm, vs *ca.* 500 nm increase at the nucleus, with an overall maximum height of 850 nm, respectively. This seems to be in accordance with the recognised mode of action of cisplatin and cisplatin-like drugs, which are known to prompt cell death mainly through apoptosis, a process that involves a series of typical morphological features such as nuclear condensation and fragmentation, and membrane disruption<sup>37</sup>. Regarding the cellular biochemical profile as probed by nano-FTIR, the proteins - mainly represented by the Amide I signal - were found to vary significantly between untreated and drug-treated cells (Figs 3 and 4). The data presently gathered evidence a very strong effect of cisplatin on the protein constituents of osteosarcoma cells, which agrees with previous studies by the authors (via micro-Raman) on the effect of cisplatin-like drugs on human triple-negative breast cancer cells<sup>6,38</sup>. Indeed, protein metalation is expected to induce conformational rearrangements, and may also trigger unfolding processes and even aggregation.

As for the cellular lipids, the spectral profile in the range between *ca.* 1400 and 1500  $\text{cm}^{-1}$  revealed noteworthy variations among drug-free and drug-exposed cells (Figs 3 and 4). Moreover, intracellular differences in the bands ascribed to lipids were detected, mainly in the drug-treated sample (Fig. 4). Within a eukaryotic cell there is a local lipid metabolism, *i.e.* lipids are synthesised according to the cellular location leading to a unique lipid composition of the different organelles<sup>38–40</sup>. Hence, such a heterogeneous cellular distribution of the different types of fatty acids (*e.g.* saturated vs unsaturated) is expected. The present results revealed a noticeable effect of cisplatin on the cellular lipidic content, which varied across the cell—mostly between the cytoplasm and the regions near to the membrane (Fig. 4B), clusters C1/C3 vs C2). This is in line with reported studies (by mass spectrometry) evidencing a significant impact of cisplatin on membrane lipids in rat tumour cells<sup>41</sup>, which is suggested to be closely linked to the cisplatin-elicited cellular apoptosis.

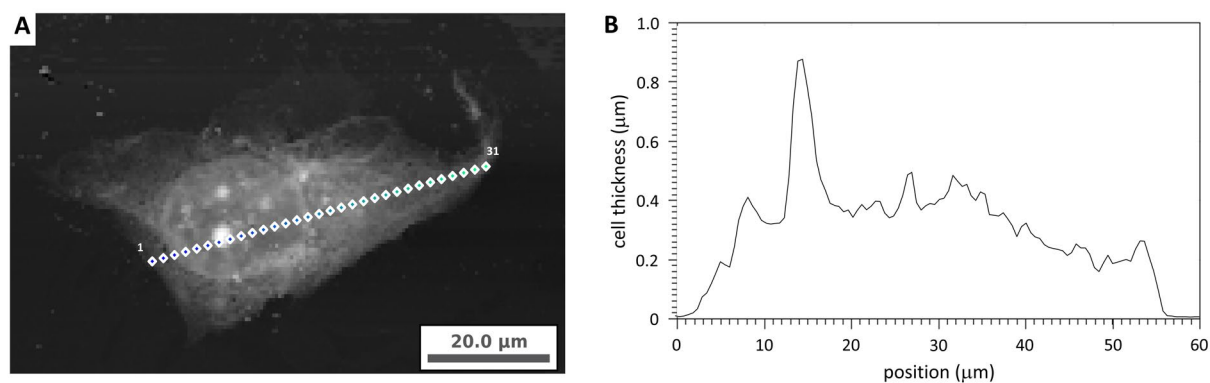


**Figure 5.** (A)—AFM topographic image of cisplatin-exposed (12  $\mu\text{M}$ , 48 h) human osteosarcoma cells (MG-63, formalin-fixed), showing the points where nano-FTIR data were collected (line scan, measuring data at every 900 nm); (B)—AFM-derived cell thickness across the scanned region.

## Conclusions

Nano-FTIR studies on cisplatin-treated human osteosarcoma cells were carried out, through s-SNOM measurement of IR *whitelight* maps and absorption spectra via broadband IR synchrotron radiation. Untreated osteosarcoma cells were also measured, as a control reference. The whole cell profile at the sub-micron (subcellular) scale was probed, yielding topographic and biochemical information which provides detailed insights into the drug's impact on the cellular metabolism. Cisplatin, as a widely used chemotherapeutic drug, showed a remarkable effect on the proteins' signal, as well as on lipids and DNA, varying according to the cellular region — either the membrane, the cytoplasm or the nucleus. Namely: i) a drug impact on protein content, mainly in the nucleus and perinuclear areas; ii) an influence on the lipids, which show a heterogeneous distribution within the cell. Overall, a major drug impact was observed on the cellular proteins, the protein-rich cytoplasm being severely affected by the presence of cisplatin. These observations are the combined outcome of a direct cisplatin interaction with the biomolecules (known to occur mainly through Pt-coordination to N and/or S atoms, *e.g.* in proteins and DNA), and of the cellular response to the chemotherapeutic insult.

With the caveat that reproducibility of nano-FTIR experiments is an open question in Life Science applications, in addition to the intrinsic biovariability across mammalian cells even from the same line, these results support the use of synchrotron nano-FTIR as a suitable nanospectroscopy probe in biomedical research, with relevance for human health through the study of drug-exposed cancer cells, since it is able to provide a label-free characterisation within the cellular milieu under different therapeutic conditions.

The new information currently gathered adds to previous data obtained on different scales by micro-FTIR and THz spectroscopies, plus micro-Raman and neutron scattering methods (inelastic and quasi-elastic)<sup>6,8–11</sup>, and goes a step further in providing a subcellular insight on the effect of the drug on specific cellular regions and biochemical components.

The methodological improvement gained through these experiments contributes to the new analytical approach offered by IR nanospectroscopy in the study of the mode of action of metalodrugs at a molecular and subcellular level, which is key for the development of improved anticancer agents, aiming at a better prognosis for oncology patients.

## Data availability

Data will be available upon request via the corresponding authors of this paper.

Received: 31 May 2024; Accepted: 10 July 2024

Published online: 26 July 2024

## References

- Cole, S., Gianferante, D. M., Zhu, B. & Mirabello, L. Osteosarcoma: A Surveillance, Epidemiology, and End Results program-based analysis from 1975 to 2017. *Cancer* **128**(11), 2107–2118 (2022).
- Rosenberg, B., Vancamp, L., Trosko, J. E. & Mansour, V. H. Platinum compounds—a new class of potent antitumour agents. *Nature* **222**(5191), 385–386 (1969).
- Rosenberg, B. & VanCamp, L. The successful regression of large solid sarcoma 180 tumors by platinum compounds. *Cancer Res.* **30**(6), 1799–1802 (1970).
- Anthony, E. J. *et al.* Metalloodrugs are unique: opportunities and challenges of discovery and development. *Chem. Sci.* **11**(48), 12888–12917 (2020).
- Ferraro, G. & Merlino, A. Metalloodrugs: Mechanisms of action, molecular targets and biological activity. *Int. J. Mol. Sci.* **23**(7), 3504 (2022).
- Batista de Carvalho, A. L. M. *et al.* Chemotherapeutic response to cisplatin-like drugs in human breast cancer cells probed by vibrational microspectroscopy. *Faraday Discuss.* **187**, 273–298 (2016).
- Marques, M. P. M., Batista de Carvalho, A. L. M., Sakai, V. G., Hatter, L. & Batista de Carvalho, L. A. E. Intracellular water—an overlooked drug target? Cisplatin impact in cancer cells probed by neutrons. *Phys. Chem. Chem. Phys.* **19**(4), 2702–2713 (2017).
- Marques, M. P. M. *et al.* Chemotherapeutic targets in osteosarcoma: Insights from synchrotron-microFTIR and quasi-elastic neutron scattering. *J. Phys. Chem. B* **123**(32), 6968–6979 (2019).
- Batista de Carvalho, A. L. M. *et al.* Anticancer drug impact on DNA—a study by neutron spectroscopy coupled with synchrotron-based FTIR and EXAFS. *Phys. Chem. Chem. Phys.* **21**(8), 4162–4175 (2019).
- Marques, M. P. M. *et al.* A new look into the mode of action of metal-based anticancer drugs. *Molecules* **25**(2), 246 (2020).
- Batista de Carvalho, L. A. E. *et al.* Metalloodrugs-protein interaction probed by synchrotron terahertz and neutron scattering spectroscopy. *Biophys. J.* **120**(15), 3070–3078 (2021).
- Knoll, B. & Keilmann, F. Near-field probing of vibrational absorption for chemical microscopy. *Nature* **399**(6732), 134–137 (1999).
- Govyadinov, A. A., Amenabar, I., Huth, F., Carney, P. S. & Hillenbrand, R. Quantitative measurement of local infrared absorption and dielectric function with tip-enhanced near-field microscopy. *J. Phys. Chem. Lett.* **4**(9), 1526–1531 (2013).
- Amenabar, I. *et al.* Structural analysis and mapping of individual protein complexes by infrared nanospectroscopy. *Nat. Commun.* **4**, 2890 (2013).
- Kaltenecker, K. J., Gözl, T., Bau, E. & Keilmann, F. Infrared-spectroscopic, dynamic near-field microscopy of living cells and nanoparticles in water. *Sci. Rep.* **11**, 21860 (2021).
- Wang, H. *et al.* Super-resolution mid-infrared spectro-microscopy of biological applications through tapping mode and peak force tapping mode atomic force microscope. *Ad. Drug Del. Rev.* **180**, 114080 (2022).
- Amrania, H. *et al.* New IR imaging modalities for cancer detection and for intra-cell chemical mapping with a sub-diffraction mid-IR s-SNOM. *Faraday Discuss.* **187**, 539 (2016).
- Lucidi, M. *et al.* SSNOMBACTER A collection of scattering-type scanning near-field optical microscopy and atomic force microscopy images of bacterial cells. *GigaScience* **9**(11), 129 (2020).
- Pereira, L. *et al.* Infrared Nanospectroscopy reveals the chemical nature of pit membranes in water-conducting cells of the plant xylem. *Plant Physiol.* **177**(4), 1629–1638 (2018).
- Ajaezi, G. C. *et al.* Near-field infrared nanospectroscopy and super-resolution fluorescence microscopy enable complementary nanoscale analyses of lymphocyte nuclei. *Analyst* **143**(24), 5926–5934 (2018).
- Bakir, G. *et al.* Ultrastructural and SINS analysis of the cell wall integrity response of *Aspergillus nidulans* to the absence of galactofuranose. *Analyst* **144**(3), 928–934 (2019).

22. Freitas, R. O. *et al.* Nano-infrared imaging of primary neurons. *Cells* **10**(10), 2559 (2021).
23. Lamego, I. *et al.* Impact of the Pd(2)spermine chelate on osteosarcoma metabolism: An NMR metabolomics study. *J. Proteome Res.* **16**(4), 1773–1783 (2017).
24. Martins, A. S. *et al.* Cytotoxicity of platinum and palladium chelates against osteosarcoma. *Chem. Select* **5**, 5993–6000 (2020).
25. Cinque, G., Frogley, M., Wehbe, K., Filik, J. & Pijanka, J. Multimode InfraRed imaging and microspectroscopy (MIRIAM) beamline at diamond. *Synchrotron. Radiat. News* **24**(5), 24–33 (2011).
26. Cinque, G. talk at *2nd International Nanoscale Analytical Workshop Munich* (2022).
27. Xu, X. G., Rang, M., Craig, I. M. & Raschke, M. B. Pushing the sample-size limit of infrared vibrational nanospectroscopy: From monolayer toward single moleculesensitivity. *J. Phys. Chem. Lett.* **3**(13), 1836–1841 (2012).
28. Berweger, S. *et al.* Nano-chemical infrared imaging of membrane proteins in lipid bilayers. *J. Am. Chem. Soc.* **135**(49), 18292–18295 (2013).
29. Toplak, M., Read, S. T., Sandt, C. & Borondics, F. Quasar: Easy machine learning for biospectroscopy. *Cells* **10**, 2300 (2021).
30. Baldassarre, L. *et al.* Mapping the amide I absorption in single bacteria and mammalian cells with resonant infrared nanospectroscopy. *Nanotechnology* **27**(7), 075101 (2016).
31. Ramer, G., Aksyuk, V. A. & Centrone, A. Quantitative chemical analysis at the nanoscale using the photothermal induced resonance technique. *Anal. Chem.* **89**(24), 13524–13531 (2017).
32. Mester, L., Govyadinov, A. A., Chen, S., Goikoetxea, M. & Hillenbrand, R. Subsurface chemical nanoidentification by nano-FTIR spectroscopy. *Nat. Commun.* **11**, 3359 (2020).
33. Bechtel, H. A., Johnson, S. C., Khatib, O., Muller, E. A. & Raschke, M. B. Synchrotron infrared nano-spectroscopy and -imaging. *Surf. Sci. Rep.* **75**(3), 100493 (2020).
34. Bellisola, G. & Sorio, C. Infrared spectroscopy and microscopy in cancer research and diagnosis. *Am. J. Cancer Res.* **2**(1), 1–21 (2012).
35. Rohman, A., Riyanto, S., Sasi, A. M. & Yusof, F. M. The use of FTIR spectroscopy in combination with chemometrics for the authentication of red fruit (*Pandanus conoideus* Lam) oil from sunflower and palm oils. *Food Biosci.* **7**, 64–70 (2014).
36. Rohman, A. *et al.* Comprehensive review on application of FTIR spectroscopy coupled with chemometrics for authentication analysis of fats and oils in the food products. *Molecules* **25**(22), 5485 (2020).
37. Saraste, A. & Pulkki, K. Morphologic and biochemical hallmarks of apoptosis. *Cardiovasc. Res.* **45**(3), 528–537 (2000).
38. Vojtek, M. *et al.* Pd(II) and Pt(II) trinuclear chelates with spermidine: selective anticancer activity towards TNBC-sensitive and -resistant to cisplatin. *Pharmaceutics* **15**(4), 1205 (2023).
39. van Meer, G., Voelker, D. R. & Feigenson, G. W. Membrane lipids: where they are and how they behave. *Nat. Rev. Mol. Cell Biol.* **9**(2), 112–124 (2008).
40. Yang, Y., Lee, M. & Fairn, G. D. Phospholipid subcellular localization and dynamics. *J. Biol. Chem.* **293**(17), 6230–6240 (2018).
41. Mohammadi, A. S., Li, X. & Ewing, A. G. Mass spectrometry imaging suggests that cisplatin affects exocytotic release by alteration of cell membrane lipids. *Anal. Chem.* **90**(14), 8509–8516 (2018).

## Acknowledgements

This work was supported by the Portuguese Foundation for Science and Technology (UIDB/00070/2020, <https://doi.org/10.54499/UIDB/00070/2020>; UIDP/00070/2020, <https://doi.org/10.54499/UIDP/00070/2020>; A.L.M.B.C. employment contract, <https://doi.org/10.54499/CEECIND/00069/2017/CP1460/CT0029>). Diamond Light Source is thanked for access via peer review (experiment SM26320-3) through the dedicated call for collaborative/commissioning beamtime at MIRIAM beamline B22.

## Author contributions

L.A.E.B.C.—conceptualisation, experimental measurements and manuscript revision; G.C.—experimental measurements, data interpretation and manuscript writing; A.L.M.B.C.—sample preparation and experimental measurements; J.M.—sample preparation and manuscript formatting; M.D.F.—experimental measurements, data analysis and manuscript writing; H.V.—experimental measurements, data analysis and manuscript writing; M.P.M.M.—conceptualisation, experimental measurements, data analysis and manuscript writing. All authors have read and agreed to the submitted version of the manuscript.

## Competing interests

The authors declare no competing interests.

## Additional information

**Supplementary Information** The online version contains supplementary material available at <https://doi.org/10.1038/s41598-024-67386-y>.

**Correspondence** and requests for materials should be addressed to G.C. or A.L.M.B.C.

**Reprints and permissions information** is available at [www.nature.com/reprints](http://www.nature.com/reprints).

**Publisher's note** Springer Nature remains neutral with regard to jurisdictional claims in published maps and institutional affiliations.





**Open Access** This article is licensed under a Creative Commons Attribution-NonCommercial-NoDerivatives 4.0 International License, which permits any non-commercial use, sharing, distribution and reproduction in any medium or format, as long as you give appropriate credit to the original author(s) and the source, provide a link to the Creative Commons licence, and indicate if you modified the licensed material. You do not have permission under this licence to share adapted material derived from this article or parts of it. The images or other third party material in this article are included in the article's Creative Commons licence, unless indicated otherwise in a credit line to the material. If material is not included in the article's Creative Commons licence and your intended use is not permitted by statutory regulation or exceeds the permitted use, you will need to obtain permission directly from the copyright holder. To view a copy of this licence, visit <http://creativecommons.org/licenses/by-nc-nd/4.0/>.

© The Author(s) 2024